

Measurement of the Hubble constant using the Dark Energy Survey Year 6 Gold galaxy catalog and the fourth Gravitational-Wave Transient Catalog

Isaac McMahon ,¹★ Danny Laghi ,¹ Marcelle Soares-Santos ,¹ Kendall Ackley ,² Gergely Dálya ,^{3,4} Yavuz Gençel ,¹ David Sánchez-Cid ,¹ Felipe Andrade-Oliveira ,¹ Sean MacBride ,¹ Christian Chapman-Bird ,⁵ Rachel Gray ,⁶ Alexander Papadopoulos ,⁶

¹Physik-Institut, University of Zürich, Winterthurerstrasse 190, 8057 Zürich, Switzerland

²Department of Physics, University of Warwick, Coventry CV4 7AL, United Kingdom

³L2IT, Laboratoire des 2 Infinis - Toulouse, Université de Toulouse, CNRS/IN2P3, UPS, F-31062 Toulouse Cedex 9, France

⁴HUN-REN-ELTE Extragalactic Astrophysics Research Group, 1117 Budapest, Hungary

⁵Institute for Gravitational Wave Astronomy & School of Physics and Astronomy, University of Birmingham, Edgbaston, Birmingham B15 2TT, UK

⁶SUPA, University of Glasgow, Glasgow G12 8QQ, United Kingdom

Accepted XXX. Received YYY; in original form ZZZ

ABSTRACT

Gravitational wave (GW) standard sirens enable independent measurements of the Hubble constant H_0 . In the absence of electromagnetic counterparts, the "dark siren" method statistically correlates GW events with potential host galaxies. We present a measurement of H_0 using 142 compact binary coalescences from the fourth Gravitational-Wave Transient Catalog (GWTC-4.0) combined with the Dark Energy Survey Year 6 Gold photometric galaxy catalog. Using the `gwcosmo` pipeline, we jointly infer cosmological and GW population parameters. We analyze the impact of galaxy catalog properties on the inference, identifying significant features in the galaxy redshift distribution which can introduce biases. By restricting the galaxy catalog to $0.05 < z < 0.35$ to maintain consistency with a uniform in comoving volume galaxy distribution, we obtain a result of $H_0 = 70.9^{+22.3}_{-18.6} \text{ km s}^{-1} \text{ Mpc}^{-1}$ from dark sirens and $H_0 = 73.1^{+11.7}_{-8.6} \text{ km s}^{-1} \text{ Mpc}^{-1}$ when combined with the bright siren GW170817. This study demonstrates the adaptation of deep galaxy catalogs for GW cosmology, highlighting key challenges and methodologies essential for maximizing the potential of next-generation galaxy surveys.

Key words: gravitational waves – catalogues – cosmological parameters – cosmology: observations

1 INTRODUCTION

The field of gravitational wave (GW) cosmology has rapidly developed alongside the growing number of GW candidate detections by the LIGO-Virgo-KAGRA (LVK) GW detector network (Abac et al. 2025e). The first part of the fourth observing run (O4a) ended on 2024 January 16, and data products from O4a were released in August 2025, bringing the number of total GW detections to 218 (Abac et al. 2025a). GWs from compact binary coalescences (CBCs) act as standard sirens (Holz & Hughes 2005), which when combined with electromagnetic observations of potential host galaxies can be used to infer cosmological parameters, such as the Hubble constant H_0 (Schutz 1986; Del Pozzo 2012). This results in a measurement of H_0 which is independent of other methodologies. With sufficient precision, GWs may help to resolve the $\gtrsim 5\sigma$ tension between H_0 measurements from the early universe (Aghanim et al. 2020) and the late universe (Riess et al. 2022).

For a given GW detection, if a unique host galaxy is positively identified through astronomical searches, the redshift of the host galaxy and the luminosity distance of the GW can be used to mea-

sure H_0 through the luminosity distance-redshift relation (Nishizawa 2017). This is known as a "bright siren", and only one such event, GW170817, has been confirmed to date (Abbott et al. 2017). In the absence of unique host galaxy identification, H_0 can still be measured by other methods, of which we consider two in this work.

One method measures H_0 from features in the GW event candidate mass spectrum, extracting information from the redshift between the source frame masses and detected masses, known as a "spectral siren" analysis (Chernoff & Finn 1993; Marković 1993; Taylor et al. 2012; Farr et al. 2019; Ezquiaga & Holz 2021; Mastrogiovanni et al. 2021; You et al. 2021; Ezquiaga & Holz 2022; Pierra et al. 2025). This method requires accurate modeling of the CBC population distribution and samples cosmological parameters alongside population parameters that describe the shape of the mass spectrum and event merger rate (Mukherjee 2022; Pierra et al. 2024; Agarwal et al. 2025).

Another method statistically weights potential host galaxies for each GW candidate, leveraging redshift information from existing galaxy catalogs (MacLeod & Hogan 2008; Gair et al. 2023; Borghi et al. 2024). This is known as the "galaxy catalog" or "dark siren" method. Recent developments in dark siren codes such as `gwcosmo` (Gray et al. 2020, 2022a, 2023) and `icarogw` (Mastrogiovanni et al. 2024) allow joint inference of cosmological parameters and GW

★ E-mail: isaac.mcmahon@physik.uzh.ch

population parameters simultaneously, combining the spectral sirens method and the galaxy catalog method into one. This combination is also referred to as the "dark siren" method, and is the one which we use in this work. Additionally, other studies have used galaxy catalogs and dark sirens to measure cosmological parameters using cross-correlation (Oguri 2016; Mukherjee & Wandelt 2018; Bera et al. 2020; Mukherjee et al. 2024).

The galaxy catalog and dark sirens method have previously been used with various galaxy catalogs, including previous data releases of the Dark Energy Survey (DES). The analyses using DES only considered a single event assuming fixed population model and merger rate parameters (Soares-Santos et al. 2019; Palmese et al. 2020) or only used DES for one event out of many (Abbott et al. 2021). Other analyses (Fishbach et al. 2019; Finke et al. 2021; Abbott et al. 2023b; Abac et al. 2025b) use GLADE or GLADE+ (Dálya et al. 2018, 2022), which is less than 50% complete at $z > 0.05$ in the K -band, too shallow to provide significant information at typical GW distances. Other analyses with the DESI (Ballard et al. 2023), DESI Legacy Survey (Palmese et al. 2023), and DELVE (Bom et al. 2024) consider only a small selection of available GW events and assume fixed mass distribution and merger rate parameters.

In this work, we adapt the DES Year 6 Gold photometric galaxy catalog (Bechtol et al. 2025) for the dark siren method and obtain an H_0 measurement with galaxies out to $z = 0.5$ (this limitation is discussed in Section 3.5). We explain our choices to make the galaxy catalog data cosmology-ready with object selection and classification (Sections 2.2 & 3.3). We measure the luminosity function of DES galaxies out to $z = 0.5$ with photometric redshift to quantify the completeness of our galaxy sample for dark sirens (Section 3.4). We describe our choices for computing the Line-of-Sight (LOS) redshift prior (Section 3.2). We present our computed LOS redshift priors and describe the features in the redshift distribution that we observe (Section 3.7). Finally, we show our measurement for H_0 and discuss potential sources of bias which arise from making different choices in the analysis (Section 4). If an assumed reference cosmology is required, we adopt best-fit values from Planck 2015 (Ade et al. 2016) unless otherwise stated, as these are the defaults used in our chosen software (see Section 3.1).

2 DATA

2.1 Gravitational-wave events

The LVK network of observatories (Abac et al. 2025e) consists of two Laser Interferometer Gravitational-Wave Observatory (LIGO; Aasi et al. 2015) detectors in the USA and the Virgo Observatory (Acernese et al. 2015) in Italy, as well as the KAGRA Observatory (Akutsu et al. 2021) in Japan. The fourth Gravitational-Wave Transient Catalog (GWTC-4.0) (Abac et al. 2025a,c,e), consisting of approximately seven months of data from 24/05/2023 to 16/01/2024, is the latest set of GW candidate data released by LVK. When combined with the previous GWTC-2.1 and GWTC-3.0 (Abbott et al. 2023a, 2024) data releases, they consist of all GW candidate data released by LVK to date. We use a candidate list which is consistent with the O4a LVK cosmology analysis (Abac et al. 2025b), totaling 142 CBC GW candidates. 137 of these candidates are believed to have an origin in a binary black hole collision, and the remaining 5 candidates could have a neutron star component. The event GW170817, one of these 5, is the only event with a confirmed electromagnetic counterpart (Coulter et al. 2017; Soares-Santos et al. 2017), and is thus treated separately in this analysis as a bright siren.

The GW information which is used as an input for our analysis comes in the form of parameter estimation posterior samples and HEALPix skymaps (Gorski et al. 2005). The posterior samples encode information obtained only from the GW signal itself, including location, mass, spin, and other parameters which affect the gravitational waveform. The skymap is created from these samples and encodes posterior probability information both on the projected celestial sphere as well as luminosity distance in the radial direction (Singer & Price 2016). For all events, we use the publicly available data released on Zenodo (relevant links found in Section 5).

In addition to the real GW candidate data, we require simulated GW injections to model GW selection effects due to detector sensitivity (Essick et al. 2025). We use the injections with simulated detector sensitivity up to O4a which were also released with GWTC-4.0.

2.2 Galaxy catalog

The Dark Energy Survey (The Dark Energy Survey Collaboration 2005; Abbott et al. 2016) was conducted using the Dark Energy Camera (DECam) at the 4-m Blanco telescope at Cerro Tololo Inter-American Observatory in Chile. The Year 6 Gold data release (Bechtol et al. 2025) is curated for cosmology analysis, covering 4923 deg² in the southern sky and achieving a photometric uniformity of < 2 mmag in the *griz* photometric filters over a total of 669 million objects. The 10σ multi-epoch galaxy magnitude depth in *r*-band is 23.9. Included in the catalog are photometric redshift (photo-z) measurements from Directional Neighborhood Fitting (DNF) (De Vicente, Sánchez & Sevilla-Noarbe 2016), with state-of-the-art average uncertainties $\sigma_z/(1+z) < 3\%$ for $z < 1$. Using the *r*-band luminosity function (see Section 3.4) and the *r*-band apparent magnitude limit, we estimate that DES is approximately 100% complete to $z \sim 0.5$ for an absolute magnitude limit $M_r < -17.5$, and complete to $z \sim 0.4$ for a limit $M_r < -17$ (Fishbach et al. 2019).

The data release includes three different models for photometric flux measurements: PSF (Point Spread Function), BDF (Bulge+Disk Fixed), and GAp (Gaussian Aperture). In this analysis we choose BDF as the representative photometry because the model performs better for galaxies. Specifically, we use the BDF_MAG_*_CORRECTED columns which have been normalized to the global MAG_APER_8 photometric calibration system and dereddened for Galactic extinction.

We apply the following recommended cuts based on quality flags for each source:

- Non-NaN redshift and photometry in the *griz* filters
- **FLAGS_FOOTPRINT == 1**
- **FLAGS_FOREGROUND == 0**
- **FLAGS_GOLD == 0**

FLAGS_FOOTPRINT is a flag that equals 1 for all sources which have data from at least 2 exposures in each of the *griz* bands, defined by a NSIDE=16384 HEALPix map of exposure areas. A cut of **FLAGS_FOOTPRINT == 1** excludes 3.3% of the full catalog. **FLAGS_FOREGROUND** is a flag for sources that are impacted by the presence of nearby bright astrophysical foreground objects. The minimum area masked by the foreground mask is the area of one HEALPix NSIDE=4096 pixel, 0.86 arcmin². A cut of **FLAGS_FOREGROUND == 0** excludes 9.7% of the full catalog. **FLAGS_GOLD** is a flag for photometric processing failures, objects with unphysical colors, noisy detections, and other issues. A cut of **FLAGS_GOLD == 0** excludes 8.1% of the full catalog. In total, these quality cuts combine to exclude 19.1% of the sources in the full catalog.

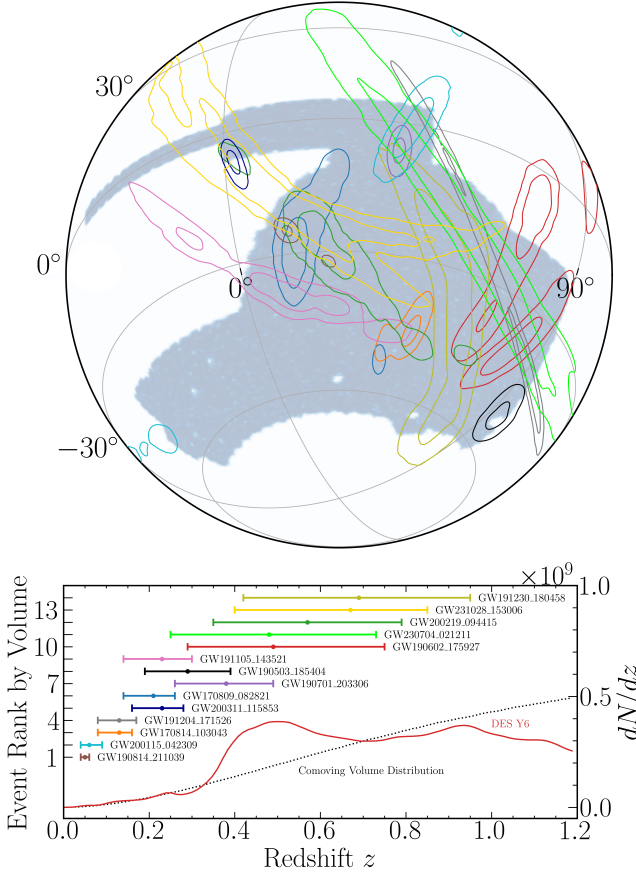


Figure 1. Top: GW event candidate 50% and 90% probability contours included in our analysis which have more than 50% probability to be within the DES Y6 Gold survey footprint (shown in blue). Bottom: The photometric redshift distribution of galaxies dN/dz in DES Y6 Gold (red) compared to a uniform in comoving volume distribution (dotted black), scaled to have the same total number of galaxies. More discussion can be found in Section 3.7. On the same x-axis are shown redshift measurements (90% confidence interval) for the events, converted from luminosity distance and ordered by increasing localization volume.

Out of all 141 GW event candidates used in our analysis as dark sirens, 14 candidates (10%) have more than 50% probability to be in the DES footprint (see Figure 1, upper panel). These candidates are well-distributed among the redshifts to which DES is most sensitive. A total of $\sim 14\%$ of the probability of all 141 candidates falls within the DES footprint or redshift depth, we still include them in our analysis as they provide crucial cosmology information mainly through the shape of the GW mass distribution.

3 METHODOLOGY

3.1 Analysis framework

We jointly infer cosmology and CBC population parameters using a Bayesian framework as implemented in the `gwcosmo` python package (Gray et al. 2022b, 2023). Given a set of GW event data $\{d\}$ from a number N_{det} of detections, θ^{det} are the parameters of the detected CBCs measured only from the GW data in the detector frame of reference. The joint posterior probability on CBC population param-

eters Λ and cosmological parameters Λ_c given a set of GW events (individually labeled with i) can thus be written as:

$$p(\Lambda, \Lambda_c | \{d\}, N_{\text{det}}) \propto \pi(\Lambda) \pi(\Lambda_c) \xi(\Lambda, \Lambda_c)^{-N_{\text{det}}} \times \prod_{i=1}^{N_{\text{det}}} \int d\theta_i^{\text{det}} \frac{p(\theta_i^{\text{det}} | d_i)}{\pi(\theta_i^{\text{det}})} \times \left| \frac{d\theta_i^{\text{det}}(\theta_i^{\text{src}}, \Lambda_c)}{d\theta_i^{\text{src}}} \right|^{-1} p(\theta_i^{\text{src}} | \Lambda) \quad (1)$$

where π denotes a prior and the GW source-frame parameters θ^{src} are given by a function of the detector-frame parameters and the cosmological parameters, $\theta^{\text{src}} = \theta(\theta^{\text{det}}, \Lambda_c)$. The term $\xi(\Lambda, \Lambda_c)$ is the expected fraction of GW events which are detected, required because the GW detectors will not be able to measure the entire true population of GW events due to some selection effects. It can be written as:

$$\xi(\Lambda, \Lambda_c) = \int d\theta^{\text{det}} P(\text{det} | \theta^{\text{det}}) \times \left| \frac{d\theta^{\text{det}}(\theta^{\text{src}}, \Lambda_c)}{d\theta^{\text{src}}} \right|^{-1} p(\theta^{\text{src}} | \Lambda) \quad (2)$$

where $P(\text{det} | \theta^{\text{det}})$ is the probability of detection given the measured GW parameters θ^{det} , dependent on the sensitivity of the detectors. The expected true underlying distribution of events $p(\theta^{\text{src}} | \Lambda)$ depends on the chosen model for the population of CBC mergers and its parameters Λ .

3.2 Line-of-sight redshift prior

In Equation 1, the probability of a set of GW parameters θ_i^{src} given Λ depends on the distribution of potential host galaxies:

$$p(\theta_i^{\text{src}} | \Lambda) \propto \frac{dN_{\text{gal,cat}}^{\text{eff}}}{dz d\Omega} + \frac{dN_{\text{gal,out}}^{\text{eff}}}{dz d\Omega} \quad (3)$$

The first term $dN_{\text{gal,cat}}^{\text{eff}}/dz d\Omega$ represents the spatial distribution of galaxies in a chosen galaxy catalog across redshift z and angular sky position Ω . Each galaxy is represented with a gaussian likelihood defined by its photometric redshift z and the redshift error σ_z at its sky location Ω . While photometric redshift uncertainties are not truly gaussian in general (Palmese et al. 2020, 2023; Turski et al. 2023; Bom et al. 2024), we use this approximation in this work.

The gaussian likelihood of each galaxy is assigned a host probability weight w_j as defined by:

$$w_j(\epsilon, M_j) = 10^{-0.4 \epsilon (M_j - M^*)} \quad (4)$$

where M^* is the reference absolute magnitude of the Schechter luminosity function, described in Section 3.4. The parameter ϵ is chosen to change how the galaxies are weighted with respect to each other. When $\epsilon = 0$, all galaxies are weighted equally as potential host galaxies for the GW event. When $\epsilon = 1$, this corresponds to a logarithmic weight in absolute magnitude, or equivalently a linear weight in luminosity. The extent to which the probability of a galaxy being a host of a CBC merger may scale with its observables is unknown and is an active field of research (Neijssel et al. 2019; Adhikari et al. 2020; Santoliquido et al. 2021; Broekgaarden et al. 2022; Rauf et al. 2023; Srinivasan et al. 2023; Hanselman et al. 2025; Li et al. 2025). As host probabilities for stellar-origin CBCs is expected to scale with the stellar mass of the galaxy, and galaxy stellar mass roughly scales with luminosity (Mobasher et al. 2015), host probabilities are expected to also scale with luminosity. Most dark siren analyses to date consider

only the cases $\epsilon = 0$ or $\epsilon = 1$, with $\epsilon = 1$ being the preferred fiducial analysis. In this work we choose $\epsilon = 1$.

The second term $dN_{\text{gal,out}}^{\text{eff}}/dzd\Omega$, known as the "empty catalog" case, represents galaxies which are assumed to exist but are not present in the catalog due to selection effects. This term is modeled by assuming that all galaxies which are not detected by the catalog follow an isotropic distribution which is uniform in comoving volume. While this does not account for galaxy clustering, we expect that this model adequately describes the real average galaxy distribution over large scales.

In `gwcosmo`, these terms are passed to the likelihood as a "Line-of-Sight (LOS) redshift prior" which encodes the sum of the in-catalog and out-of-catalog terms as a probability distribution in redshift for every pixel in a `HEALPix` map of chosen resolution (Gray et al. 2022b). For each pixel, only the cataloged galaxies in that pixel contribute to the probability distribution. This LOS redshift prior is unique for each galaxy catalog, and so is the focus of this work. We compute the LOS redshift prior for DES Year 6 Gold using `gwcosmo` and use it to obtain the posterior probability distributions on the population parameters Λ and cosmological parameters Λ_c .

The spacing of the redshift array used in the calculation of the redshift prior and the dark siren likelihood must be chosen to allow for sufficient resolution to capture information from every galaxy considering its redshift error. The spacing between consecutive elements of the array must be smaller than the smallest redshift errors in the catalog at that redshift. We adopt a redshift array that satisfies these conditions for the properties of the DES catalog, with a linear spacing of 4.4×10^{-4} for $0 < z \leq 0.5$, then logarithmic from $0.5 < z < 10$ to a maximum spacing of 8.9×10^{-3} .

3.3 Galaxy catalog choices

Several choices must be made before computing the LOS redshift prior for DES Y6 Gold. We choose to use r -band photometry because the average photometric magnitude errors in r are smaller than in the other three bands.

The catalog provides two morphological classifiers to remove stars from our sample, the discrete-valued flag `EXT_MASH` (based on `SourceExtractor` (Bertin & Arnouts 1996) shape measurement outputs) and the continuous-valued `XGB_PRED` (made using the gradient boosted decision tree machine learning algorithm `XGBoost` (Chen & Guestrin 2016)). While `EXT_MASH == 4` is the recommended fiducial classifier choice used in DES cosmological analyses, we use the object classification cut `EXT_XGB == 4`, defined as a cut at the value of `XGB_PRED` which passes the same number of objects as `EXT_MASH == 4`. This is because `XGBoost` classification performs better for objects with bright apparent magnitudes. Bright stars which are misclassified as galaxies will have large, spurious luminosities. This has an outsized impact on the dark siren redshift prior when luminosity weighting is used, causing large weights to be assigned to objects which are not galaxies.

While DES Y6 Gold has high completeness out to $z \sim 1$, we find that the photometric redshift distribution of galaxies in the catalog does not well follow our assumption of uniform in comoving volume in a region centered around $z \sim 0.5$ (see Figure 1, bottom panel). Because of the limited precision of photometric redshift estimation, it is unclear if this deviation is indicative of real structure in the galaxy distribution or systematic biases in redshift estimation. For this reason we apply a redshift cut z_{max} which excludes all in-catalog contribution to the redshift prior for $z > z_{\text{max}}$. We compute the redshift prior for several different values of $z > z_{\text{max}}$ to determine the impact of the

galaxy distribution on the resulting posterior distribution. We further discuss the features in the galaxy redshift distribution in Section 3.7.

Additionally, objects begin to saturate in the DECam sensors at apparent magnitudes of $m_r < 16$, meaning that objects which appear brighter than this are not cataloged in DES Y6 Gold. This saturation effect disproportionately affects galaxies at redshifts $z < 0.05$. For this reason we also apply a redshift cut on the low end of the LOS redshift prior at $z_{\text{min}} = 0.05$, excluding all in-catalog contribution to the redshift prior below this redshift. For all redshifts outside of the interval defined by the redshift cuts, $z_{\text{min}} < z < z_{\text{max}}$, the redshift prior consists only of the out-of-catalog term and follows exactly a uniform in comoving volume distribution. This has the added benefit of avoiding the need for bulk peculiar velocity corrections for the catalog, as these corrections are only valid for redshifts $z < 0.05$ and are anyway of an order much smaller than typical photometric redshift errors (Mukherjee et al. 2021). No events in the DES footprint have the majority of their localization volume below $z < 0.05$, although two events have their localization volumes near the cut. As the comoving volume assumption is used in the cut region, the lost information does not bias the resulting measurement.

We choose a `HEALPix` resolution of `NSIDE=128`. For this resolution, pixels in the DES footprint have $\mathcal{O}(10^{2-3})$ galaxies between the chosen redshift cuts compared to $\mathcal{O}(10^{0-1})$ for `GLADE+`. Beyond this resolution, the improvement in the posterior from better resolution is marginal because the posterior is more limited by GW data precision than galaxy catalog precision. We also adopt the same resolution for the coarse-resolution maps of the magnitude threshold m_{thr} and effective galaxy number N_{eff} which are used for calculation of the redshift prior, as our galaxy density allows us to be robust against small-number statistics even at such resolution.

3.4 Luminosity function

The galaxy luminosity function, in the form of the Schechter function (Schechter 1976), is used in the calculation of the redshift prior to find the completeness fraction of the galaxy catalog at a given redshift, which is used in the out-of-catalog term of Equation 3. The Schechter function in terms of absolute magnitude takes the form:

$$\Phi(M) dM = 0.4 \ln(10) \phi^* 10^{0.4(\alpha+1)(M^*-M)} \times \exp \left[-10^{0.4(M^*-M)} \right] dM \quad (5)$$

where ϕ^* , M^* , and α are empirical characteristic parameters which describe the shape of the luminosity function. These parameters are passed as inputs to `gwcosmo` to compute the LOS redshift prior, along with the maximum and minimum magnitudes, M_{max} and M_{min} , which determine the interval on which the Schechter parameterization is trustworthy.

The galaxy luminosity function is known to evolve as a function of redshift (Blanton et al. 2003; Loveday et al. 2011). In `gwcosmo`, the input Schechter parameters are taken at face value for the entire redshift range with no evolution correction model assumed or applied. For this reason, we must model Schechter evolution effects separately and choose a redshift for which we evaluate the Schechter parameters which we use to compute the redshift prior. We model the evolution effects to be linear in redshift and take the forms:

$$\begin{aligned} M^*(z) &= M_0^* + Q_M(z - z_0), \\ \alpha(z) &= \alpha_0 + Q_\alpha(z - z_0), \\ \phi^*(z) &= \phi_0^* 10^{P_\phi(z - z_0)} \end{aligned} \quad (6)$$

where Q_M , Q_α , and P_ϕ are evolutionary parameters and z_0 is a zeropoint redshift against which the parameters are corrected. There have been several studies in the last few decades which measure Schechter function parameters for the r -band (Blanton et al. 2003; Montero-Dorta & Prada 2009; Hill et al. 2010; Loveday et al. 2011), but all of these studies either ignore evolution effects, do not cover our desired redshift range, or report only the "true" Schechter parameters at z_0 after correcting for evolution over the entire redshift range. For this reason, we empirically measure the Schechter parameters from DES Y6 Gold and use these to compute the redshift prior.

To measure the luminosity function, we adopt the $1/V_{\max}$ method (Eales 1993). We define the luminosity function Φ for a redshift range $z_1 < z < z_2$ to take the form:

$$\int_{M_1}^{M_2} \Phi \, dM = \sum_i^N \frac{1}{V_{\max,i}} \quad (7)$$

for an absolute magnitude bin with edges M_1 and M_2 which contains N galaxies. The maximum accessible comoving volume for the i th galaxy $V_{\max,i}$ is defined as:

$$V_{\max,i} = A_{\text{cat}} \left[\frac{c}{H_0} \int_{z_{\text{gal,min},i}}^{z_{\text{gal,max},i}} \frac{dz'}{\sqrt{\Omega_m(1+z')^3 + (1-\Omega_m)}} \right]^3 \quad (8)$$

where A_{cat} is the solid angle subtended by the galaxy catalog, c is the speed of light, $H_0 = 100 h$ is the Hubble constant, and Ω_m is the cosmological matter density parameter. For measuring the luminosity function, it is customary to set $H_0 = 100 \text{ km s}^{-1} \text{ Mpc}^{-1}$ ($h = 1$), as the measured Schechter parameters can be easily converted to different H_0 .

The limits of integration in Equation 8 define the maximum redshift range of the i th galaxy given the absolute magnitude of the galaxy and are defined as:

$$z_{\text{gal,min},i} = \max(z_1, z_{\text{bright},i}), \quad z_{\text{gal,max},i} = \min(z_2, z_{\text{faint},i}) \quad (9)$$

where $z_{\text{bright},i}$ and $z_{\text{faint},i}$ are the redshifts for which a galaxy of absolute magnitude M would have an apparent magnitude of the bright- and faint-end apparent magnitude limits of the galaxy catalog, taken for DES Y6 Gold to be $m_{\text{faint},r} = 23.9$ and $m_{\text{bright},r} = 14$. The absolute magnitude M , apparent magnitude m , and z of a given galaxy are related to each other by:

$$M_r = m_r - 5 \log_{10} \left[\frac{D_L}{10 \text{ pc}} \right] - K(z) \quad (10)$$

where D_L is the luminosity distance:

$$D_L = \frac{c(1+z)}{H_0} \int_0^z \frac{dz'}{\sqrt{\Omega_m(1+z')^3 + (1-\Omega_m)}} \quad (11)$$

and K is the K correction, described in Section 3.5. To estimate errors on the luminosity function, we subdivide the galaxy catalog into 20 subregions using a k -means clustering algorithm (Kwan et al. 2016; Suchyta et al. 2016) to measure variations over the footprint of the survey, adjusting A_{cat} accordingly. To approximate the error in the luminosity function due to photometric redshift error, we conduct many realizations of the luminosity function measurement, resampling the redshift of each galaxy with an added random gaussian shift scaled by the σ_z of that galaxy. We compute the mean and standard deviation value of Φ across all realizations and subregions for each magnitude bin and fit the Schechter function to these values.

We use this method to estimate the Schechter parameters of DES

Y6 Gold and their evolution over the redshift range $0.05 < z < 0.5$, shown in Figure 2 and Table 1. To determine the Schechter parameters to use to compute the redshift prior for each z_{\max} , we evaluate the Schechter parameters according to the linear evolution fit at the median redshift of all galaxies with $z < z_{\max}$. We define M_{\min} as the location of the most bright M bin that does not have any galaxies in it. We define M_{\max} as the location of the peak of the luminosity function distribution for $M < -17$. Because we expect the luminosity function to monotonically increase for fainter M , any downturn in the measured luminosity function in the faint end must be due to selection effects and is therefore not a reliable measurement.

Our measurements are generally consistent with previous studies. We note that the evolution of α is poorly constrained and is often not modeled in such analyses. There have been some studies which suggest that α decreases as redshift increases, due to the redshift evolution of galaxy morphology (Ellis et al. 1996; Ilbert et al. 2005).

3.5 K corrections

The K correction in Equation 10 accounts for the shifting of the observed spectrum of a galaxy at redshift z , causing the portion of the spectrum which is detected by a given photometric filter to be different between the rest and observed frames (Hogg et al. 2002). In order to directly compare the absolute magnitudes of the galaxies in the rest frame, the magnitudes must be K-corrected. We adopt a polynomial fit of K corrections in redshift and color space (Chilengarian, Melchior & Zolotukhin 2010), allowing us to compute any K correction for r -band given z and $g-r$ color. These K corrections are only reliable for $z < 0.5$ and $-0.1 < g-r < 1.9$, imposed by the wavelength coverage of the chosen survey filters. For this reason, we only consider values of $z_{\max} \leq 0.5$ in this work. The constraint imposed by K correction calculations of $z < 0.5$ excludes $\sim 80\%$ of the galaxies in DES, but this exclusion accounts for only $\sim 24\%$ of the cumulative localization volume of all GW events up to GWTC-4.0 in the DES footprint. While the inclusion of higher redshift galaxies would further constrain H_0 , the bulk of H_0 constraining power comes from $z < 0.5$.

The K correction polynomials were originally fit to SDSS photometric filters, which slightly differ from DECam filters. Because of this, we convert the DECam magnitudes to SDSS magnitudes for all galaxies following a set of transformations defined by DES (Drlica-Wagner et al. 2018).

3.6 Hardware acceleration of `gwcosmo`

Previous large-scale analyses using `gwcosmo`, such as those in Abac et al. (2025b), have exclusively been performed via parallel processing over central processing unit (CPU) cores. However, as the number of included GW events grows, inference rapidly becomes computationally infeasible (with analyses of ~ 200 events taking $\gtrsim 1$ week distributed over 32 CPU cores). This high computational cost is mainly due to the need to evaluate kernel density estimates (KDEs) over θ^{src} for all sky-pixels associated with each GW event, which is necessary to compute the integral in Equation 1. As θ^{src} change for each new likelihood evaluation, these KDEs must be constructed on the fly. As open-source tools for parallel KDE construction are not available, `gwcosmo` computes them sequentially, leading to further inefficiencies.

In this work, we employ a new version of `gwcosmo` that both addresses this limitation and accelerates each likelihood evaluation with vectorization on graphics processing unit (GPU) hardware. The key

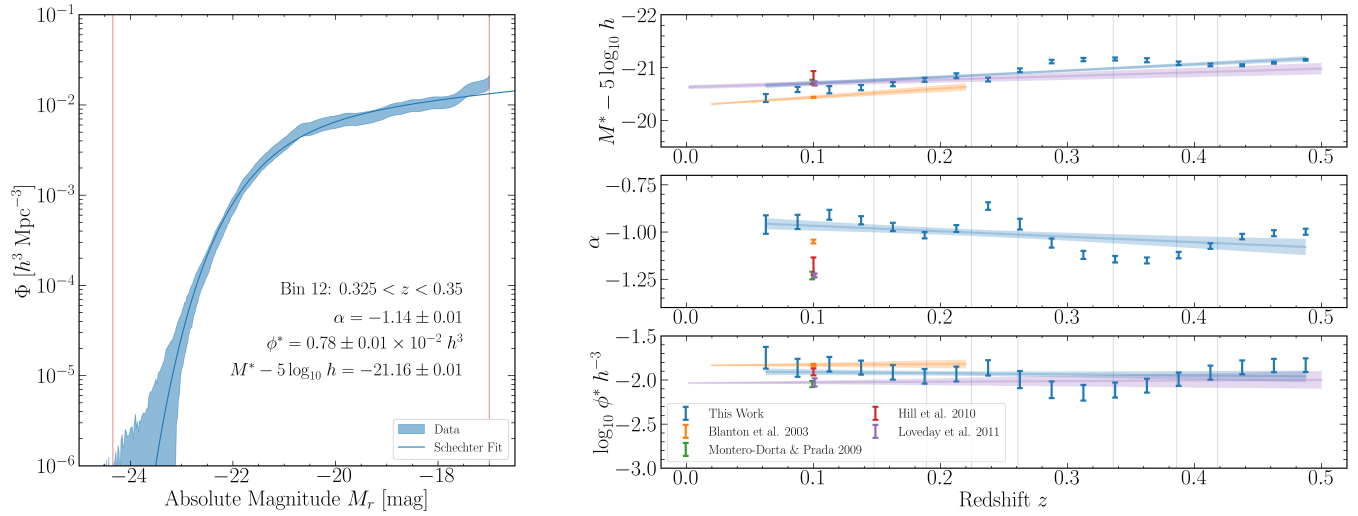


Figure 2. *Left:* Luminosity function with 1σ errors and corresponding Schechter function fit in the example redshift range $0.325 < z < 0.35$. M_{\min} and M_{\max} are shown in red. *Right:* r -band Schechter function parameters as a function of redshift and their linear evolution fits. Results from the literature are shown for comparison with evolution when included, typically measured using $z_0 = 0.1$ (Blanton et al. 2003; Montero-Dorta & Prada 2009; Hill et al. 2010; Loveday et al. 2011). The vertical blue lines indicate the different values of z_{median} , given in the second column of Table 1.

Table 1. Measured Schechter parameters for every z_{max}

z_{max}	z_{median}	ϕ^* $10^{-2} h^3 \text{ Mpc}^{-3}$	$M^* - 5 \log_{10} h$ mag	α	M_{\min} mag	M_{\max} mag
0.20	0.148	1.21 ± 0.08	-20.76 ± 0.03	-0.98 ± 0.02	-23.89	-17.33
0.25	0.189	1.20 ± 0.07	-20.81 ± 0.03	-0.99 ± 0.02	-24.17	-17.86
0.30	0.224	1.18 ± 0.07	-20.85 ± 0.03	-1.00 ± 0.02	-24.21	-18.24
0.35	0.261	1.17 ± 0.08	-20.90 ± 0.02	-1.01 ± 0.02	-24.29	-16.33
0.40	0.336	1.15 ± 0.10	-20.99 ± 0.03	-1.04 ± 0.02	-24.35	-16.98
0.45	0.386	1.13 ± 0.12	-21.05 ± 0.03	-1.05 ± 0.03	-24.82	-17.45
0.50	0.418	1.12 ± 0.14	-21.08 ± 0.04	-1.06 ± 0.03	-24.92	-17.73

structural change necessary to achieve this is to operate directly on a large three-dimensional array of posterior samples (with each axis referring to the event, pixel or posterior sample index respectively). As each pixel contains a different number of posterior samples, we pad the excess entries with NaNs. This layout allows for high-level operations on posterior samples that can be easily expressed as array operations (e.g., parameter transformations, selection effect estimation and population model evaluation) to be performed with the hardware-accelerated PyTorch computational framework (Paszke et al. 2019), using NaN-aware operations where required. To maximize efficiency and limit memory consumption, we vectorize the KDE evaluation and subsequent integration of Equation 1 with custom CUDA kernels, which we implement via the CUDA target of the Numba library (Lam, Pitrou & Seibert 2015). These kernels leverage low-level operations and shared memory usage to operate directly over the (non-padded) posterior samples, circumventing the instantiation of large intermediate arrays and minimizing wasted computations.

These improvements typically yield a speed-up of 1–2 orders of magnitude over a cluster of 32 CPU cores, depending on the number of GW events; this reduces analysis wall-times from days to hours, enabling `gwcosmo` to scale to GW catalogs of hundreds (or even thousands) of events. Further details of the hardware acceleration of `gwcosmo` will be presented in a forthcoming work (Papadopoulos, Chapman-Bird & Gray, in prep.).

3.7 LOS prior validation

The resulting LOS redshift priors calculated for different values of z_{max} , averaged over the DES footprint, are shown in Figure 3. Although the galaxy catalog on average is expected to align closely with the comoving volume assumption, we find that the prior constructed from the galaxy catalog presents various features across the considered redshift ranges. We find that the maximum deviation of the average prior from a comoving volume distribution increases from 13% with $z_{\text{max}} = 0.20$ to 18% with $z_{\text{max}} = 0.35$ to 41% with $z_{\text{max}} = 0.50$.

Some of these redshift features have been observed before and noted in previous dark siren studies. Earlier versions of the DES catalog were used in single-event analyses of GW170814 (Soares-Santos et al. 2019) and GW190814 (Palmese et al. 2020), which found that a "galaxy wall" overdensity structure exists in the DES footprint, spanning the region $35 < \alpha < 55$ and $-55 < \delta < -35$ and centered at $z \sim 0.06$. A similar peak was observed at $z \sim 0.12$. These features persist across multiple photometric redshift estimation algorithms and are also confirmed by several spectroscopic surveys of the region (Shectman et al. 1996; Colless et al. 2001; Jones et al. 2009), suggesting that these are real structures.

The overdensity of galaxies in the DES catalog at $0.35 < z < 0.65$ (see Figure 1) is clearly visible in the priors which include that redshift range. As the distribution of in-catalog galaxies in the first

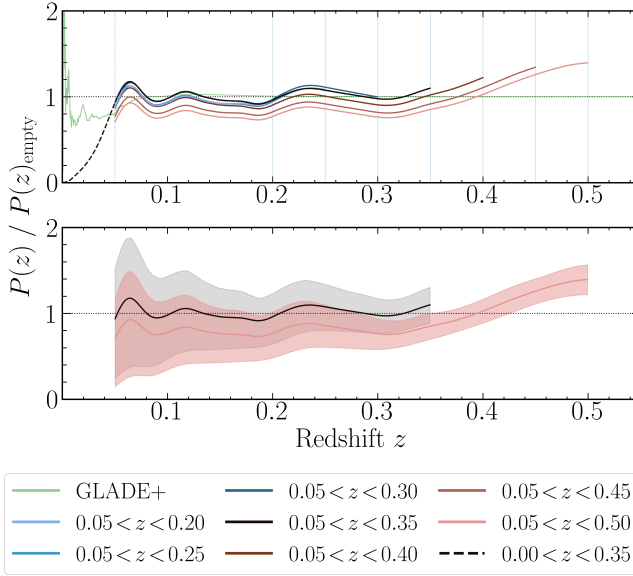


Figure 3. *Top:* LOS redshift priors averaged over the footprint of the DES survey, calculated for different choices of upper redshift cut. For the regions $z < z_{\min}$ and $z > z_{\max}$, the prior reverts to the default uniform in comoving volume "Empty" catalog assumption. The y-axis is the ratio between the catalog prior and the empty catalog. The chosen values of z_{\max} and z_{\min} are shown as blue vertical lines, as in Figure 1. The average LOS redshift prior for GLADE+ K -band is shown in green for comparison. The effect of applying a cut at z_{\min} is shown for $z_{\max} = 0.35$ with a dashed line at low redshift. If there is no cut, the prior dramatically decreases at low redshift due to the saturation selection effect. *Bottom:* 1σ average redshift prior comparison for $z_{\max} = 0.35, 0.50$. For $z_{\max} \leq 0.35$, each prior is entirely within 1σ of the empty catalog. All $z_{\max} \geq 0.40$ exceed 1σ at some point.

term of Equation 3 is normalized, this overdensity also reduces the contribution of the galaxies compared to the empty catalog term, even at lower redshifts. As the construction of the LOS prior relies heavily on the assumption that galaxies are distributed uniformly in comoving volume on average, this means that large observed deviations from this assumption in the catalog degrade the integrity of the resulting prior.

The source of this large overdensity is unclear. The feature is present in the SDSS BOSS spectroscopic galaxy catalog (Ahn et al. 2014), which was used as a training redshift set for photometric redshift algorithms in DES, including DNF (De Vicente et al. 2016). The BOSS galaxy distribution was composed from two different target selection algorithms, one designed for $0.15 < z < 0.4$ and the other for $0.4 < z < 0.8$ (Ahn et al. 2012). In between these two selections at $z \sim 0.45$, difficulties in photometric redshift estimation resulted in a 25% lower galaxy density at that redshift. These difficulties persist across many different photometric redshift estimators (Sánchez et al. 2014). Ultimately, all of these issues exist in the redshift sample used to train DES redshifts and may be projected onto the inferred galaxy distribution. The feature does not exist in the first DESI data spectroscopic data release (Abdul-Karim et al. 2025a), although that survey has not reached its target depth and has a different spectroscopic targeting selection function which results in a galaxy density deficit at $z \sim 0.5$.

Large deviations from the assumption cause large step features at the z_{\max} boundary, where the in-catalog term sharply transitions to the out-of-catalog term. While this step feature is indicative of biases in the construction of the catalog which may affect the inference of

H_0 , the presence of the step feature itself does not add additional bias if it is within acceptable limits. This is because the likelihood calculation of the posterior is not sensitive to discontinuities in the redshift slope.

Because the dark siren methodology used in this work relies on the assumption that galaxies are distributed evenly in comoving volume, we take our fiducial result to be the LOS redshift prior with the highest z_{\max} that does not deviate more than 1σ away from a uniform in comoving volume distribution for all z . Among our calculated priors, all with $z_{\max} \leq 0.35$ pass this criterion, while all with $z_{\max} \geq 0.40$ fail. This means that $z_{\max} = 0.35$ is our fiducial cut.

4 RESULTS

Using our calculated LOS priors, we run `gwcosmo` to obtain joint posterior sample distributions for H_0 and GW population parameters, using the GW event catalog and injections outlined in Section 2.1. For our mass population model, we use the `FULLPOP-4.0` (Abac et al. 2025d), which infers parameters of both neutron-star and black-hole populations at once. We assume Madau-Dickinson merger rate evolution (Madau & Dickinson 2014) and unmodified General Relativity. We used the `nessai` nested sampler with normalizing flows (Williams et al. 2021, 2023) with 1500 live points and default settings. We use identical priors for all parameters as those used in Abac et al. (2025b). We also conduct spectral siren and GLADE+ runs to recover previous results. We report the results for H_0 in Table 2. More information about the mass model and results for all sampled parameters, including mass model parameters, can be found in Appendix A.

The resulting posterior distributions are shown in Figure 4. The bulk of the constraining power for all priors comes from the coupling of cosmology to features in the mass spectrum of all the events, meaning that all the results from the galaxy catalogs currently provide only a slight improvement to the empty catalog spectral sirens case. This is because the galaxy catalogs are either too narrow or too shallow to provide much galaxy distribution information for most of the GW events in the sample. As galaxy catalogs improve, so will the cosmology constraints from dark sirens.

All DES posteriors have similar results, aside from minor deviations for the extreme cases of z_{\max} . For $z_{\max} = 0.20$, the catalog is too shallow to provide much additional constraint. For $z_{\max} = 0.40, 0.45, 0.50$, the divergence from a uniform in comoving volume galaxy distribution results in a lateral shift in the peak value of H_0 , which can be understood as correlation between GW events which have support for redshifts $z \gtrsim 0.5$ and the redshift prior peak at the near side of their confidence volume, resulting in lower H_0 values.

We also show the effect of applying z_{\min} to avoid selection effects from saturation in Figure 5. In general, the deweighting of the prior at $z < z_{\min}$ causes the corresponding values of H_0 to be similarly deweighted, pushing the measured peak of the H_0 distribution to higher redshifts.

Figure 6 shows our final estimate for dark sirens and standard sirens. For the dark sirens only (with $0.05 < z < 0.35$) we obtain a measurement of $H_0 = 70.9^{+22.3}_{-18.6}$ (black solid line), representing a $\sim 13\%$ improvement in precision over O4a dark sirens with GLADE+. We combine our results with the bright siren GW170817 posterior publicly released with the LVK O4a cosmology results and obtain a combined fiducial standard sirens measurement of $H_0 = 73.1^{+11.7}_{-8.6}$, representing a $\sim 5\%$ improvement in precision over the O4a standard siren result.

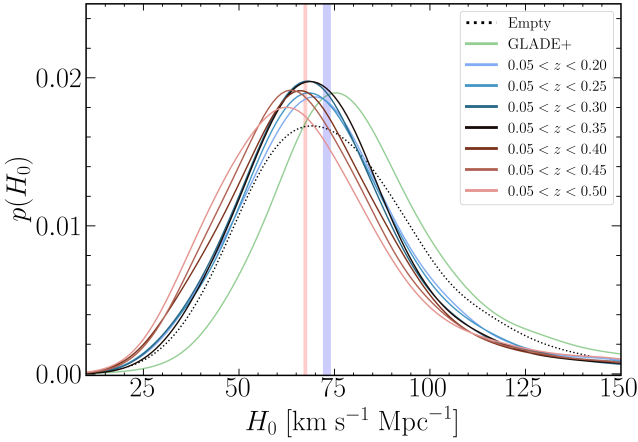


Figure 4. Posterior distributions for different choices of z_{\max} . The result for the dark siren analysis using GLADE+ K -band is shown in green. The "empty catalog" spectral siren result is shown with a dotted line. 1σ regions for early- and late- universe H_0 measurements are shown in red and blue, respectively (Aghanim et al. 2020; Riess et al. 2022).

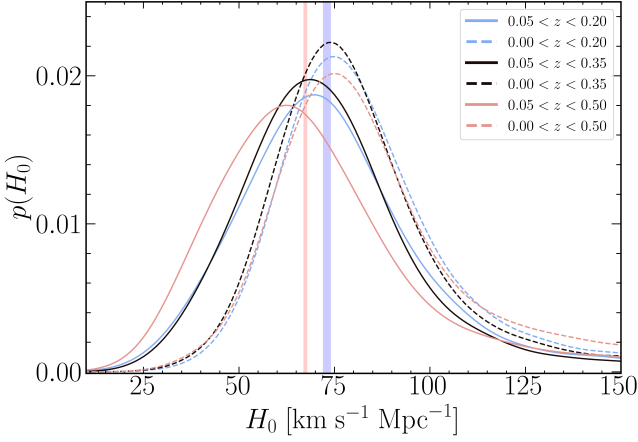


Figure 5. Posterior distributions with and without the use of z_{\min} , shown for $z_{\max} = 0.20, 0.35, 0.50$ as example. 1σ regions for early- and late- universe H_0 measurements are again shown in red and blue.

5 CONCLUSIONS

In this work we demonstrate the use of large galaxy catalogs for joint dark siren analysis with cosmology and population parameters by making relevant object cuts and measuring the luminosity function. Analyzing 141 GW events up to GWTC-4.0 as dark sirens with the DES Year 6 Gold galaxy catalog, we obtain a result of $H_0 = 70.9^{+22.3}_{-18.6} \text{ km s}^{-1} \text{ Mpc}^{-1}$ and $H_0 = 73.1^{+11.7}_{-8.6} \text{ km s}^{-1} \text{ Mpc}^{-1}$ when combined with the bright siren GW170817, using the FULLPOP-4.0 mass model and assuming host galaxy weighting by luminosity. This represents a $\sim 13\%$ improvement over the LVK cosmology dark siren analysis with GWTC-4.0 and the GLADE+ galaxy catalog and a $\sim 5\%$ improvement when combined with GW170817. We show the importance of catalog redshift depth by obtaining a competitive result with a galaxy catalog that covers $\sim 13\%$ of the full sky and has a galaxy density of the order $O(10^{2-3})$ times greater than GLADE+.

We find that because of limitations imposed by calculating K corrections with the observed survey filters, we must exclude galaxies

Table 2. Posterior statistics for H_0 with 1σ (68.3%) confidence intervals

Catalog	z_{\min}	z_{\max}	H_0 $\text{km s}^{-1} \text{ Mpc}^{-1}$
DES	0.05	0.20	$72.1^{+24.6}_{-19.9}$
DES	0.05	0.25	$71.4^{+24.8}_{-19.1}$
DES	0.05	0.30	$70.2^{+23.1}_{-18.6}$
DES	0.05	0.35	$70.9^{+22.3}_{-18.6}$
DES	0.05	0.40	$68.3^{+24.1}_{-19.7}$
DES	0.05	0.45	$66.9^{+24.9}_{-18.9}$
DES	0.05	0.50	$65.7^{+26.9}_{-19.8}$
DES	0.00	0.20	$79.5^{+25.2}_{-15.8}$
DES	0.00	0.35	$77.5^{+23.2}_{-15.5}$
DES	0.00	0.50	$79.8^{+30.1}_{-16.7}$
Empty	–	–	$74.5^{+27.3}_{-20.7}$
GLADE+	–	–	$79.6^{+27.3}_{-18.5}$
GW170817	–	–	$78.2^{+26.0}_{-11.8}$
DES + GW170817	0.05	0.35	$73.1^{+11.7}_{-8.6}$

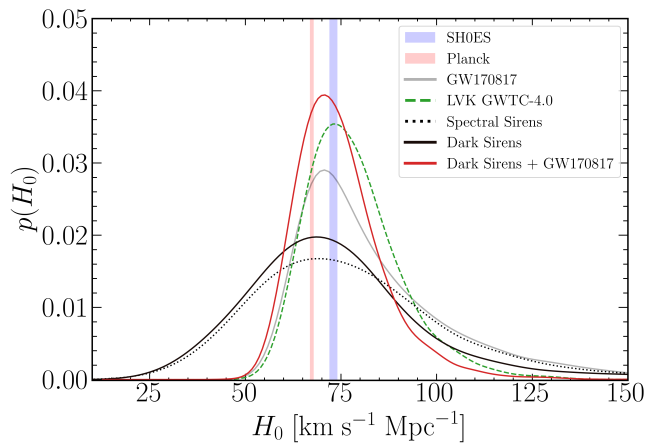


Figure 6. The final standard siren result of this work, the dark siren posterior for $z_{\max} = 0.35$ combined with the bright siren posterior for GW170817, is shown in red. The equivalent fiducial combined result from LVK O4a for GLADE+ is shown in green (Abac et al. 2025b). 1σ regions for SH0ES and Planck (Aghanim et al. 2020; Riess et al. 2022) are also shown.

with redshift $z > 0.5$. Furthermore, we further impose a galaxy cut to $0.05 < z < 0.35$ due to CCD saturation effects at low redshift and a deviation from a uniform in comoving volume galaxy distribution at higher redshifts possibly induced by photo-z estimation artifacts. We show the effects of imposing these cuts on the resulting H_0 posterior. Additionally, DES only covers $\sim 13\%$ of the sky, limiting the overlap of GW events with the galaxy catalog. We use a global Schechter function parameterization that is corrected for evolution based on the median redshift of galaxies in the given sample instead of smoothly modeling the Schechter evolution inside the LOS prior calculation. The evolution of the luminosity function with redshift is a lower-order effect that nonetheless has important implications for the LOS prior (Turiski et al. 2025).

Multiple unprecedented wide-field galaxy surveys are scheduled to be released in the next few years, such as DESI DR2 (Abdul Karim

et al. 2025b), LSST (Ivezic et al. 2019), Euclid (Amendola et al. 2018), and 4MOST (Verdier et al. 2025). The amount of galaxy data that is useful for dark sirens in both area and depth will soon grow immensely. The last two data releases for the fourth LVK observing run (O4) are expected to be released before the end of 2026 (Arnaud 2025). Plans for the fifth LVK observing run (O5) are not yet finalized but are expected to begin in late 2027 with major upgrades to all detectors, yielding even more GW detections, possibly including more bright siren candidates. For these reasons, this work and future improvements will be instrumental to prepare for the era of precision GW cosmology with these future releases.

ACKNOWLEDGEMENTS

Funding for this work is provided by the University of Zurich (UZH) and the Swiss National Science Foundation (SNSF) under grant number 10002981. DL is supported by the UZH Postdoc Grant, grant no. [K-72341-01-01]. CEAC-B acknowledges support from UKSA grant UKRI971. AP is supported by UKRI STFC studentship 323353-01. We thank Benoit Revenu for advice on analysis input parameters and use of `gwcosmo`. We thank the LVK Cosmology working group for the productive discussions throughout the development of this work. This work made use of infrastructure services provided by the UZH Science IT team (www.s3it.uzh.ch). This material is based upon work supported by NSF's LIGO Laboratory which is a major facility fully funded by the National Science Foundation. This project used public archival data from the Dark Energy Survey (DES). Funding for the DES Projects has been provided by the DOE and NSF(USA), MEC/MICINN/MINECO(Spain), STFC(UK), HEFCE(UK). NCSA(UIUC), KICP(U. Chicago), CCAPP(Ohio State), MIFPA(Texas A&M), CNPQ, FAPERJ, FINEP (Brazil), DFG(Germany) and the DES Collaborating Institutions. Based in part on observations at Cerro Tololo Inter-American Observatory, NOIRLAB, which is operated by the Association of Universities for Research in Astronomy (AURA) under a cooperative agreement with the NSF.

DATA AVAILABILITY

The DES Y6 Gold galaxy catalog can be accessed at NCSA¹, CosmoHub², or NOIRLab³. GLADE+ can be accessed at its dedicated website⁴. GW parameter estimation samples can be downloaded on Zenodo for GWTC-4.0⁵, GWTC-3.0⁶, and GWTC-2.1⁷, as well as the injections used to model the GW selection effect⁸ and cosmology posterior samples and distributions from the LVK O4a cosmology analysis⁹. We make use of the `gwcosmo` python package¹⁰. All other code or data produced for this work can be shared upon reasonable request to the corresponding author.

¹ <https://des.ncsa.illinois.edu/releases/y6a2/Y6gold>

² <https://cosmohub.pic.es/catalogs/333>

³ <https://datalab.noirlab.edu/>

⁴ <https://glade.elte.hu/>

⁵ <https://zenodo.org/records/17014085>

⁶ <https://zenodo.org/records/8177023>

⁷ <https://zenodo.org/records/6513631>

⁸ <https://zenodo.org/records/16740128>

⁹ <https://zenodo.org/records/16919645>

¹⁰ <https://git.ligo.org/lscsoft/gwcosmo>

REFERENCES

Aasi J., et al., 2015, *Class. Quantum Gravity*, 32, 074001
 Abac A. G., et al., 2025b, pre-print arXiv:2509.04348
 Abac A. G., et al., 2025c, arXiv:2508.18081
 Abac A. G., et al., 2025d, pre-print arXiv:2508.18083
 Abac A. G., et al., 2025a, arXiv:2508.18082
 Abac A. G., et al., 2025e, *ApJL*, 995, L18
 Abbott T., et al., 2016, *MNRAS*, 460, 1270–1299
 Abbott B. P., et al., 2017, *Nature*, 551, 85–88
 Abbott B. P., et al., 2021, *ApJ*, 909, 218
 Abbott R., et al., 2023a, *Phys. Rev. X*, 13
 Abbott R., et al., 2023b, *ApJ*, 949, 76
 Abbott R., et al., 2024, *Phys. Rev. D*, 109
 Abdul-Karim M., et al., 2025a, pre-print arXiv:2503.14745
 Abdul Karim M., et al., 2025b, *Phys. Rev. D*, 112
 Acernese F., et al., 2015, *Class. Quantum Gravity*, 32, 024001
 Ade P. A. R., et al., 2016, *A&A*, 594, A13
 Adhikari S., Fishbach M., Holz D. E., Wechsler R. H., Fang Z., 2020, *ApJ*, 905, 21
 Agarwal A., et al., 2025, *ApJ*, 987, 47
 Aghanim N., et al., 2020, *A&A*, 641, A6
 Ahn C. P., et al., 2012, *ApJS*, 203, 21
 Ahn C. P., et al., 2014, *ApJS*, 211, 17
 Akutsu T., et al., 2021, *Prog. Theor. Exp. Phys.*, 2021, 05A101
 Amendola L., et al., 2018, *Living Rev. Relativ.*, 21
 Arnaud N., 2025, in LVK update for OpenMMA call. <https://dcc.ligo.org/LIGO-G2500315/public>
 Ballard W., et al., 2023, *RNAAS*, 7, 250
 Bechtol K., et al., 2025, arXiv:2501.05739
 Bera S., Rana D., More S., Bose S., 2020, *ApJ*, 902, 79
 Bertin E., Arnouts S., 1996, *A&AS*, 117, 393–404
 Blanton M. R., et al., 2003, *ApJ*, 592, 819
 Bom C. R., Alfradique V., Palmese A., Teixeira G., Santana-Silva L., Santos A., Darc P., 2024, *MNRAS*, 535, 961–975
 Borghi N., Mancarella M., Moresco M., Tagliazucchi M., Iacobelli F., Cimatti A., Maggiore M., 2024, *ApJ*, 964, 191
 Broekgaarden F. S., et al., 2022, *MNRAS*, 516, 5737–5761
 Chen T., Guestrin C., 2016, in Proc. 22nd ACM SIGKDD Int. Conf. Knowledge Discovery Data Mining. KDD '16. ACM, New York, NY, USA, p. 785–794, doi:10.1145/2939672.2939785
 Chernoff D. F., Finn L. S., 1993, *ApJ*, 411, L5
 Chilingarian I., Melchior A. L., Zolotukhin I., 2010, *MNRAS*, 405, 1409
 Colless M., et al., 2001, *MNRAS*, 328, 1039–1063
 Coulter D. A., et al., 2017, *Science*, 358, 1556–1558
 De Vicente J., Sánchez E., Sevilla-Noarbe I., 2016, *MNRAS*, 459, 3078–3088
 Del Pozzo W., 2012, *Phys. Rev. D*, 86
 Drlica-Wagner A., et al., 2018, *ApJS*, 235, 33
 Dálya G., et al., 2018, *MNRAS*, 479, 2374–2381
 Dálya G., et al., 2022, *MNRAS*, 514, 1403–1411
 Eales S., 1993, *ApJ*, 404, 51
 Ellis R. S., Colless M., Broadhurst T., Heyl J., Glazebrook K., 1996, *MNRAS*, 280, 235–251
 Essick R., et al., 2025, *Phys. Rev. D*, 112
 Ezquiaga J. M., Holz D. E., 2021, *ApJL*, 909, L23
 Ezquiaga J. M., Holz D. E., 2022, *Phys. Rev. Lett.*, 129
 Farah A., Fishbach M., Essick R., Holz D. E., Galaudage S., 2022, *ApJ*, 931, 108
 Farr W. M., Fishbach M., Ye J., Holz D. E., 2019, *ApJL*, 883, L42
 Finke A., Foffa S., Iacobelli F., Maggiore M., Mancarella M., 2021, *JCAP*, 2021, 026
 Fishbach M., et al., 2019, *ApJL*, 871, L13
 Fishbach M., Essick R., Holz D. E., 2020, *ApJL*, 899, L8
 Gair J. R., et al., 2023, *AJ*, 166, 22
 Gorski K. M., Hivon E., Banday A. J., Wandelt B. D., Hansen F. K., Reinecke M., Bartelmann M., 2005, *ApJ*, 622, 759–771
 Gray R., et al., 2020, *Phys. Rev. D*, 101, 122001
 Gray R., Messenger C., Veitch J., 2022a, *MNRAS*, 512, 1127

Gray R., Messenger C., Veitch J., 2022b, *MNRAS*, 512, 1127–1140
 Gray R., et al., 2023, *JCAP*, 2023, 023
 Hanselman A. G., Vijaykumar A., Fishbach M., Holz D. E., 2025, *ApJ*, 979, 9
 Hill D. T., Driver S. P., Cameron E., Cross N., Liske J., Robotham A., 2010, *MNRAS*
 Hogg D. W., Baldry I. K., Blanton M. R., Eisenstein D. J., 2002, [arXiv:astro-ph/0210394](https://arxiv.org/abs/astro-ph/0210394)
 Holz D. E., Hughes S. A., 2005, *ApJ*, 629, 15
 Ilbert O., et al., 2005, *A&A*, 439, 863–876
 Ivezić Z., et al., 2019, *ApJ*, 873, 111
 Jones D. H., et al., 2009, *MNRAS*, 399, 683–698
 Kwan J., et al., 2016, *MNRAS*, 464, 4045–4062
 Lam S. K., Pitrou A., Seibert S., 2015, in Proc. 2nd Workshop LLVM Compiler Infrastructure HPC. LLVM '15. ACM, New York, NY, USA, [doi:10.1145/2833157.2833162](https://doi.org/10.1145/2833157.2833162)
 Li Z., Gray R., Heng I. S., 2025, pre-print [arXiv:2508.15574](https://arxiv.org/abs/2508.15574)
 Loveday J., et al., 2011, *MNRAS*, 420, 1239–1262
 MacLeod C. L., Hogan C. J., 2008, *Phys. Rev. D*, 77
 Madau P., Dickinson M., 2014, *ARA&A*, 52, 415–486
 Mali U., Essick R., 2025, *ApJ*, 980, 85
 Marković D., 1993, *Phys. Rev. D*, 48, 4738–4756
 Mastrogiovanni S., et al., 2021, *Phys. Rev. D*, 104
 Mastrogiovanni S., et al., 2024, *A&A*, 682, A167
 Mobasher B., et al., 2015, *ApJ*, 808, 101
 Montero-Dorta A. D., Prada F., 2009, *MNRAS*, 399, 1106–1118
 Mukherjee S., 2022, *MNRAS*, 515, 5495–5505
 Mukherjee S., Wandelt B. D., 2018, [arXiv:1808.06615](https://arxiv.org/abs/1808.06615)
 Mukherjee S., Lavaux G., Bouchet F. R., Jasche J., Wandelt B. D., Nissanke S., Leclercq F., Hotokezaka K., 2021, *A&A*, 646, A65
 Mukherjee S., Krolewski A., Wandelt B. D., Silk J., 2024, *ApJ*, 975, 189
 Neijssel C. J., et al., 2019, *MNRAS*, 490, 3740–3759
 Nishizawa A., 2017, *Phys. Rev. D*, 96
 Oguri M., 2016, *Phys. Rev. D*, 93
 Palmese A., et al., 2020, *ApJL*, 900, L33
 Palmese A., Bom C. R., Mucesh S., Hartley W. G., 2023, *ApJ*, 943, 56
 Paszke A., et al., 2019, [arXiv:1912.01703](https://arxiv.org/abs/1912.01703)
 Pierra G., Mastrogiovanni S., Perriès S., Mapelli M., 2024, *Phys. Rev. D*, 109
 Pierra G., Colombo A., Mastrogiovanni S., 2025, pre-print [arXiv:2511.11795](https://arxiv.org/abs/2511.11795)
 Rauf L., Howlett C., Davis T. M., Lagos C. D. P., 2023, *MNRAS*, 523, 5719–5737
 Riess A. G., et al., 2022, *ApJL*, 934, L7
 Santoliquido F., Mapelli M., Giacobbo N., Bouffanais Y., Artale M. C., 2021, *MNRAS*, 502, 4877–4889
 Schechter P., 1976, *ApJ*, 203, 297
 Schutz B. F., 1986, *Nature*, 323, 310–311
 Shectman S. A., Landy S. D., Oemler A., Tucker D. L., Lin H., Kirshner R. P., Schechter P. L., 1996, *ApJ*, 470, 172
 Singer L. P., Price L. R., 2016, *Phys. Rev. D*, 93
 Soares-Santos M., et al., 2017, *ApJL*, 848, L16
 Soares-Santos M., et al., 2019, *ApJL*, 876, L7
 Srinivasan R., Lamberts A., Bizouard M. A., Bruel T., Mastrogiovanni S., 2023, *MNRAS*, 524, 60–75
 Suchyta E., et al., 2016, *MNRAS*, 457, 786–808
 Sánchez C., et al., 2014, *MNRAS*, 445, 1482–1506
 Taylor S. R., Gair J. R., Mandel I., 2012, *Phys. Rev. D*, 85, 023535
 The Dark Energy Survey Collaboration 2005, [arXiv:astro-ph/0510346](https://arxiv.org/abs/astro-ph/0510346)
 Turski C., Bilicki M., Dálya G., Gray R., Ghosh A., 2023, *MNRAS*, 526, 6224–6233
 Turski C., Brozzetti M. L., Dálya G., Punturo M., Ghosh A., 2025, pre-print [arXiv:2505.13568](https://arxiv.org/abs/2505.13568)
 Verdier A., et al., 2025, *MNRAS*, 545
 Williams M. J., Veitch J., Messenger C., 2021, *Phys. Rev. D*, 103
 Williams M. J., Veitch J., Messenger C., 2023, *Mach. Learn.: Sci. Technol.*, 4, 035011
 You Z. Q., Zhu X. J., Ashton G., Thrane E., Zhu Z. H., 2021, *ApJ*, 908, 215

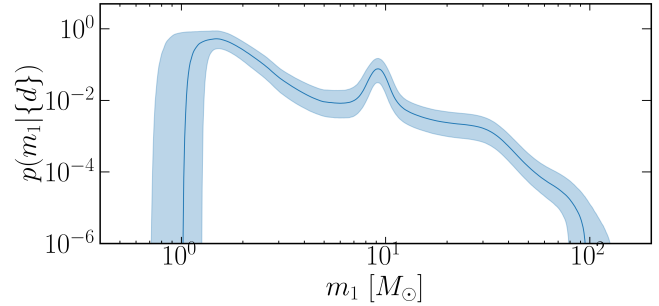


Figure A1. Reconstructed source-frame primary mass distribution for the fiducial $z_{\max} = 0.35$ with 1σ (68.3%) confidence interval, assuming the FULLPop-4.0 CBC mass model.

APPENDIX A: ADDITIONAL POSTERIOR PARAMETERS

We adopt the FULLPop-4.0 model for the distribution of primary CBC masses. This is a phenomenological model that combines theoretical expectations with previous GW observations to parameterize the distributions of both black holes and neutron stars in CBCs (Fishbach et al. 2020; Farah et al. 2022; Mali & Essick 2025). The model features two separate power law components for neutron stars and black holes, two gaussian peaks within the black hole region, and a dip at the apparent mass gap between neutron stars and black holes. In total, there are nineteen parameters in the mass model. More detail about the definitions, priors, and construction of the parameters can be found in Abac et al. (2025b).

The shape of the mass model with the parameters sampled in our fiducial result can be seen in Figure A1. The measured values for all sampled parameters are found in Table A1. Almost all of the parameters change very little with different catalogs and analysis choices, with the exception of the parameters which describe the position of the limits and peaks of the mass spectrum (m_{\max} , μ_g^{low} , and μ_g^{high}). This is because these are the parameters which have the highest correlation with H_0 . Otherwise, we find a high degree of consistency between our results and previous studies.

This paper has been typeset from a \TeX / \LaTeX file prepared by the author.

Table A1. Full posterior parameter results with 1σ (68.3%) confidence intervals

Catalog	z_{\min}	z_{\max}	H_0 km s $^{-1}$ Mpc $^{-1}$	γ	z_p	κ	α_1	α_2	β_1	β_2
DES	0.05	0.20	$72.1^{+24.6}_{-19.9}$	$3.36^{+0.76}_{-0.66}$	$2.52^{+0.96}_{-0.99}$	$2.9^{+2.0}_{-1.9}$	$2.93^{+1.19}_{-0.91}$	$1.65^{+0.34}_{-0.46}$	$1.11^{+0.60}_{-0.48}$	$2.49^{+0.62}_{-0.53}$
DES	0.05	0.25	$71.4^{+24.8}_{-19.1}$	$3.35^{+0.78}_{-0.66}$	$2.51^{+0.98}_{-0.97}$	$3.0^{+2.0}_{-2.0}$	$2.83^{+1.14}_{-0.92}$	$1.68^{+0.31}_{-0.41}$	$1.11^{+0.59}_{-0.49}$	$2.51^{+0.65}_{-0.53}$
DES	0.05	0.30	$70.2^{+23.1}_{-18.6}$	$3.39^{+0.81}_{-0.67}$	$2.47^{+1.02}_{-0.99}$	$2.9^{+2.1}_{-2.0}$	$2.91^{+1.17}_{-0.92}$	$1.66^{+0.32}_{-0.42}$	$1.14^{+0.59}_{-0.49}$	$2.51^{+0.64}_{-0.53}$
DES	0.05	0.35	$70.9^{+22.3}_{-18.6}$	$3.36^{+0.77}_{-0.64}$	$2.48^{+1.00}_{-0.98}$	$2.9^{+2.0}_{-2.0}$	$2.89^{+1.19}_{-0.93}$	$1.66^{+0.32}_{-0.42}$	$1.11^{+0.59}_{-0.48}$	$2.50^{+0.64}_{-0.51}$
DES	0.05	0.40	$68.3^{+24.1}_{-19.7}$	$3.38^{+0.84}_{-0.65}$	$2.44^{+1.01}_{-0.99}$	$3.0^{+2.0}_{-2.0}$	$2.98^{+1.12}_{-0.92}$	$1.65^{+0.31}_{-0.42}$	$1.10^{+0.58}_{-0.48}$	$2.52^{+0.62}_{-0.53}$
DES	0.05	0.45	$66.9^{+24.9}_{-18.9}$	$3.34^{+0.79}_{-0.69}$	$2.49^{+0.97}_{-0.99}$	$3.0^{+2.0}_{-2.0}$	$2.93^{+1.20}_{-0.95}$	$1.65^{+0.31}_{-0.42}$	$1.14^{+0.60}_{-0.49}$	$2.48^{+0.64}_{-0.52}$
DES	0.05	0.50	$65.7^{+26.9}_{-19.8}$	$3.41^{+0.83}_{-0.70}$	$2.36^{+1.00}_{-0.94}$	$3.0^{+2.0}_{-2.0}$	$2.87^{+1.16}_{-0.91}$	$1.68^{+0.31}_{-0.41}$	$1.14^{+0.57}_{-0.49}$	$2.47^{+0.64}_{-0.52}$
Empty	–	–	$74.5^{+27.3}_{-20.7}$	$3.36^{+0.75}_{-0.63}$	$2.46^{+1.00}_{-0.95}$	$2.8^{+2.1}_{-1.9}$	$2.95^{+1.22}_{-0.94}$	$1.65^{+0.34}_{-0.44}$	$1.12^{+0.61}_{-0.49}$	$2.53^{+0.66}_{-0.53}$
GLADE+	–	–	$79.6^{+27.3}_{-18.5}$	$3.27^{+0.72}_{-0.61}$	$2.53^{+0.97}_{-0.96}$	$2.9^{+2.0}_{-2.0}$	$3.03^{+1.20}_{-0.94}$	$1.64^{+0.35}_{-0.46}$	$1.13^{+0.59}_{-0.47}$	$2.55^{+0.66}_{-0.53}$

m_{\min} M_{\odot}	m_{\max} M_{\odot}	λ_g	λ_g^{low}	μ_g^{low} M_{\odot}	σ_g^{low}	μ_g^{high} M_{\odot}	σ_g^{high}	δ_m^{max} M_{\odot}	δ_m^{min} M_{\odot}	A
$1.00^{+0.25}_{-0.31}$	$97.0^{+40.0}_{-17.4}$	$0.22^{+0.13}_{-0.09}$	$0.69^{+0.09}_{-0.10}$	$8.91^{+0.52}_{-0.82}$	$0.84^{+0.52}_{-0.27}$	$25.1^{+3.7}_{-5.4}$	$9.6^{+3.5}_{-3.1}$	$0.11^{+1.92}_{-0.10}$	$0.08^{+0.25}_{-0.06}$	$0.48^{+0.28}_{-0.31}$
$0.99^{+0.26}_{-0.33}$	$99.1^{+47.0}_{-18.9}$	$0.22^{+0.13}_{-0.09}$	$0.69^{+0.09}_{-0.10}$	$8.97^{+0.49}_{-0.74}$	$0.81^{+0.46}_{-0.25}$	$25.3^{+3.6}_{-5.5}$	$9.6^{+3.6}_{-3.2}$	$0.05^{+1.17}_{-0.05}$	$0.07^{+0.23}_{-0.05}$	$0.45^{+0.29}_{-0.29}$
$0.99^{+0.26}_{-0.32}$	$97.6^{+40.4}_{-17.8}$	$0.21^{+0.13}_{-0.09}$	$0.69^{+0.08}_{-0.10}$	$9.00^{+0.49}_{-0.73}$	$0.84^{+0.45}_{-0.27}$	$25.3^{+3.6}_{-5.3}$	$9.6^{+3.5}_{-3.1}$	$0.09^{+1.61}_{-0.09}$	$0.08^{+0.25}_{-0.06}$	$0.46^{+0.28}_{-0.30}$
$0.99^{+0.25}_{-0.32}$	$96.6^{+40.8}_{-16.8}$	$0.21^{+0.12}_{-0.09}$	$0.69^{+0.08}_{-0.10}$	$8.98^{+0.48}_{-0.69}$	$0.81^{+0.47}_{-0.26}$	$25.1^{+3.7}_{-5.1}$	$9.6^{+3.5}_{-3.1}$	$0.04^{+0.46}_{-0.04}$	$0.08^{+0.27}_{-0.06}$	$0.45^{+0.28}_{-0.29}$
$1.00^{+0.25}_{-0.31}$	$98.6^{+40.8}_{-17.7}$	$0.22^{+0.12}_{-0.09}$	$0.68^{+0.09}_{-0.10}$	$9.06^{+0.49}_{-0.69}$	$0.82^{+0.42}_{-0.25}$	$25.0^{+3.9}_{-5.4}$	$10.2^{+3.3}_{-3.3}$	$0.08^{+1.32}_{-0.07}$	$0.07^{+0.21}_{-0.05}$	$0.43^{+0.29}_{-0.29}$
$1.00^{+0.26}_{-0.32}$	$98.0^{+37.2}_{-17.3}$	$0.21^{+0.12}_{-0.09}$	$0.69^{+0.08}_{-0.10}$	$9.04^{+0.51}_{-0.78}$	$0.85^{+0.50}_{-0.27}$	$25.5^{+3.7}_{-5.3}$	$9.7^{+3.5}_{-3.1}$	$0.08^{+1.59}_{-0.07}$	$0.08^{+0.27}_{-0.06}$	$0.46^{+0.29}_{-0.29}$
$0.99^{+0.26}_{-0.32}$	$99.8^{+40.2}_{-18.0}$	$0.21^{+0.12}_{-0.08}$	$0.69^{+0.08}_{-0.10}$	$9.07^{+0.52}_{-0.78}$	$0.85^{+0.48}_{-0.27}$	$25.5^{+3.8}_{-5.4}$	$9.9^{+3.4}_{-3.1}$	$0.07^{+1.43}_{-0.07}$	$0.08^{+0.26}_{-0.06}$	$0.46^{+0.28}_{-0.29}$
$1.01^{+0.24}_{-0.33}$	$97.5^{+43.3}_{-18.1}$	$0.22^{+0.13}_{-0.09}$	$0.68^{+0.09}_{-0.10}$	$8.90^{+0.52}_{-0.75}$	$0.82^{+0.46}_{-0.26}$	$24.4^{+3.9}_{-5.5}$	$10.0^{+3.4}_{-3.3}$	$0.10^{+1.84}_{-0.09}$	$0.07^{+0.22}_{-0.05}$	$0.44^{+0.29}_{-0.29}$
$0.98^{+0.26}_{-0.32}$	$95.0^{+46.6}_{-18.0}$	$0.21^{+0.13}_{-0.09}$	$0.68^{+0.09}_{-0.11}$	$8.79^{+0.48}_{-0.81}$	$0.80^{+0.50}_{-0.25}$	$24.2^{+3.8}_{-5.9}$	$9.6^{+3.6}_{-3.2}$	$0.03^{+0.20}_{-0.02}$	$0.07^{+0.22}_{-0.05}$	$0.45^{+0.29}_{-0.29}$

m_d^{low} M_{\odot}	m_d^{high} M_{\odot}	δ_d^{low} M_{\odot}	δ_d^{high} M_{\odot}
$2.23^{+0.51}_{-0.49}$	$7.4^{+1.1}_{-1.8}$	$0.13^{+0.63}_{-0.11}$	$0.10^{+0.36}_{-0.08}$
$2.24^{+0.53}_{-0.50}$	$7.1^{+1.3}_{-1.6}$	$0.10^{+0.54}_{-0.08}$	$0.12^{+0.69}_{-0.10}$
$2.23^{+0.52}_{-0.49}$	$7.2^{+1.3}_{-1.6}$	$0.13^{+0.59}_{-0.10}$	$0.16^{+0.75}_{-0.13}$
$2.22^{+0.53}_{-0.49}$	$7.2^{+1.3}_{-1.7}$	$0.12^{+0.53}_{-0.09}$	$0.15^{+0.71}_{-0.12}$
$2.25^{+0.52}_{-0.50}$	$7.0^{+1.4}_{-1.5}$	$0.10^{+0.47}_{-0.08}$	$0.14^{+0.74}_{-0.11}$
$2.24^{+0.53}_{-0.50}$	$7.1^{+1.3}_{-1.6}$	$0.11^{+0.50}_{-0.08}$	$0.15^{+0.73}_{-0.12}$
$2.24^{+0.52}_{-0.50}$	$7.2^{+1.2}_{-1.6}$	$0.12^{+0.59}_{-0.10}$	$0.12^{+0.63}_{-0.10}$
$2.25^{+0.51}_{-0.51}$	$7.2^{+1.2}_{-1.6}$	$0.13^{+0.64}_{-0.11}$	$0.12^{+0.63}_{-0.10}$
$2.26^{+0.51}_{-0.51}$	$7.3^{+1.2}_{-1.7}$	$0.13^{+0.66}_{-0.10}$	$0.12^{+0.68}_{-0.10}$